

REGULAR PAPER

Effect of sulfur doping on the photocatalytic performance of sputtered BiVO_4 thin films

To cite this article: Shukur Gofurov *et al* 2023 *Jpn. J. Appl. Phys.* **62** SK1051

View the [article online](#) for updates and enhancements.

You may also like

- [Enriched Photoelectrochemical Performance of Phosphate Doped \$\text{BiVO}_4\$ Photoelectrode by Coupling \$\text{FeOOH}\$ and \$\text{rGO}\$](#)
Qin Shi, Xiaozhe Song, Hui Wang et al.
- [Surface decoration of \$\text{BiOCl}\$ with \$\text{BiVO}_4\$ particles towards enhanced visible-light-driven photocatalytic performance](#)
Jialei Huang, Min Lai, Jinyu Yang et al.
- [Visible-light-driven photocatalytic removal of \$\text{Cr\(VI\)}\$ and rhodamine B by monoclinic \$\text{BiVO}_4\$ -diatomite composite](#)
Liguang Xiao, Genzhuang Li, Xuefeng Chu et al.



Effect of sulfur doping on the photocatalytic performance of sputtered BiVO₄ thin films

Shukur Gofurov^{1,2} , Namiki Uezono¹, Lingga Ghufira Oktariza¹, Jiaqi Liu¹, Sachin Pawar¹, Muhammad M. Islam^{1,3} , and Takeaki Sakurai^{1*}

¹Faculty of Pure and Applied Sciences, University of Tsukuba, Tsukuba 305-8573, Ibaraki, Japan

²Uzbekistan-Japan Innovation Center of Youth, Tashkent 100180, Uzbekistan

³Alliance for Research on the Mediterranean and North Africa (ARENA), University of Tsukuba, Tsukuba 305-8573, Ibaraki, Japan

*E-mail: sakurai@bk.tsukuba.ac.jp

Received December 25, 2022; revised April 2, 2023; accepted May 10, 2023; published online June 8, 2023

BiVO₄ thin films doped with various concentrations of sulfur were fabricated using RF sputtering followed by post-deposition sulfurization. The incorporation of sulfur in the samples was calculated to be approximately 8–11 at% from the S2s peak in their X-ray photoelectron spectra. The optical bandgap of sulfur-doped BiVO₄ was generally smaller than that of the undoped sample. BiVO₄ films doped with ~8 at% sulfur showed the highest photoelectrochemical performance compared to the undoped sample. Almost similar minority-carrier lifetimes in undoped and low sulfur-doped BiVO₄, measured by time resolve photoluminescence, suggest that the crystal qualities in terms of the recombination properties are roughly the same for both cases. Thus, although further investigation may be necessary, the improved photocurrent in 8 at% sulfur-doped BiVO₄ in our study can roughly be attributed to the decrease in the bandgap, which facilitates more photoexcited carriers to contribute to the photoelectrochemical reaction. A further increase in sulfur doping above 10 at% distorted the BiVO₄ local crystal structure, inducing defects, thus resulting in a lower photocurrent. © 2023 The Japan Society of Applied Physics

Supplementary material for this article is available [online](#)

1. Introduction

Currently, the focus is on developing numerous renewable energy sources, including new materials for photovoltaic energy and solar hydrogen production. A promising method of generating solar hydrogen energy has been photoelectrochemical (PEC) water-splitting using semiconductor materials since TiO₂ was first realized as a photoanode in 1972.¹⁾ TiO₂ has a limitation: the wide bandgap (3.0–3.2 eV) of this photoanode allows it to operate only under UV light irradiation.²⁾ Several semiconductor materials (for example, WO₃,³⁾ BiVO₄,⁴⁾ and Fe₂O₃⁵⁾) have been reported as photoanodes; however, none of the metal oxides have yet demonstrated potential for use in practical applications.⁶⁾ Bismuth vanadate (BiVO₄) is a promising photoanode light absorber because of its narrow bandgap, non-toxicity, high stability, and excellent photocatalytic effect.^{6–11)} The photocatalytic water oxidation properties of BiVO₄ were first discovered by Kudo et al.¹²⁾ The monoclinic scheelite phase of the material proved that it is an efficient water oxidation photocatalyst. Monoclinic BiVO₄ has a relatively narrower bandgap (2.4–2.5 eV) compared to other metal oxide photoanode candidates that utilize more photon energy.¹³⁾ The conduction band of BiVO₄ is mainly composed of V3d, and the VB is formed by the hybrid orbitals of Bi6s and O2p, driving hole-transport to the surface.^{12,14)} Despite its good photocatalytic activity, unmodified BiVO₄ has not yet achieved its best efficiency with the limitation of a relatively wide bandgap. Excited electrons have less energy than ~2.48 eV and cannot obtain a conduction band and recombine with holes fast. To circumvent this limitation, various methods for optimization of BiVO₄, including doping, have been developed. Most studies have been focused on molybdenum and tungsten cation dopants with the goal of substituting vanadium sites.^{15–19)} In addition, anion doping with sulfur is a possible approach to enhance the charge-carrier mobility by decreasing the BiVO₄ bandgap.²⁰⁾ Cation doping might result

in a downward shift of the conduction band which recedes from the water reduction potential position.²¹⁾ Sulfur has higher orbital energy than oxygen, and the substitution of oxygen with sulfur in BiVO₄ shifts the VB upward, resulting in a decrease in its bandgap. Experimentally, the substitution of oxygen with sulfur might be difficult, because the bonding energy of metals (or non-metals) with oxygen is higher than their bonding energy with sulfur (for example, V–O, 637 kJ mol⁻¹; V–S, 449 kJ mol⁻¹ at 298 K).²¹⁾ A few studies on sulfur doping of BiVO₄ thin films using various methods have been reported.^{20–23)} This study is focused on sulfur doping of BiVO₄ to enhance the thin-film PEC performance using the RF sputtering method and post-sulfurization. First, BiVO₄ thin films were deposited using RF sputtering. Sulfur-doped BiVO₄ films were obtained by the post-sulfurization process with the advantage of simple control of the doping concentration of sulfur into BiVO₄ thin films.

2. Experimental methods

2.1. Thin-film preparation

BiVO₄ thin films were deposited by RF sputtering. A BiVO₄ target (consisting of Bi₂O₃ and V₂O₅ in a 1: 2 molar ratio) was used as the sputtering source. The RF power for sputtering was set to 50 W. The O₂ partial pressure (defined as O₂/Ar+O₂) was set at 5%, while the total pressure was maintained at 0.6 Pa during sputtering. BiVO₄ thin films were deposited on alkaline Earth boro-aluminosilicate glass (Eagle XG, Corning) and fluorine-doped tin oxide (FTO, TEC7, Sigma-Aldrich, Louis, MO, USA) substrates, for optical measurements and structural analysis, PEC measurements, respectively. The deposited BiVO₄ thin films on glass and FTO substrates were placed in a gold-coated tubular furnace and annealed at 500 °C for 90 min under an O₂ atmosphere of 10⁵ Pa to obtain monoclinic BiVO₄ crystal structures.

2.2. Sulfurization

The sulfurization process was used to incorporate sulfur into the BiVO₄ thin films, as the schematic illustration shows in Fig. 1(a).

The sulfur powder was placed alongside the BiVO_4 samples in a graphite box (internal size: 10 cm \times 2 cm \times 0.6 cm). Sulfur powder (250, 500, and 750 mg) was used to incorporate sulfur of various concentrations into the BiVO_4 thin films. Subsequently, a graphite box was introduced into the annealing furnace. The temperature was increased from 20 $^\circ\text{C}$ to 350 $^\circ\text{C}$ by 10 $^\circ\text{C}$ min^{-1} . After maintaining the temperature at 350 $^\circ\text{C}$ for 60 min, the heating was stopped, and the sample was naturally cooled. During sulfurization, 10^5 Pa nitrogen gas flow was maintained in the annealing furnace. Sulfur-doped BiVO_4 samples on FTO substrates with various colors, compared to BiVO_4 , are shown in Fig. 1(b). The names of the samples were chosen according to the atomic percentage of sulfur in the BiVO_4 thin films, calculated from the X-ray photoelectron spectroscopy (XPS) results.

2.3. Characterization

The chemical states and compositions of the BiVO_4 and sulfur-doped BiVO_4 thin films on the FTO substrate were determined by XPS (JPS-9010 series, JEOL). The atomic ratios of S, Bi, V, and O were calculated by the peak area considering sensitive factors. The C1s peak (284.8 eV) was used for calibration. Structural analysis of the BiVO_4 and sulfur-doped BiVO_4 films was performed using X-ray diffraction (XRD; X'Pert, Malvern PANalytical) analysis and Raman spectroscopy (Nanofinder 30, Tokyo Instruments). Raman spectra were measured using a 532 nm Nd:YAG laser source. Transmittance and reflectance spectra were obtained using a UV-vis/NIR spectrophotometer (V-670, Jasco).

Steady-state photoluminescence (PL) spectra of pure and sulfur-doped BiVO_4 thin films on FTO substrate were measured at 298 K with different wavelength sources: 532 nm excitation line from Nd:YAG laser source (J100GS, SOC) and 400 nm laser light, which is a second harmonic generation of 800 nm excitation light from a Ti:sapphire femtosecond laser source (model 3986, Spectra-Physics). A CCD detector (iDus 401 Series, ANDOR) was used for the Raman and PL spectra. RT time-resolved photoluminescence (TRPL) was measured from a 400 nm excitation pulsed light with a pulse width and repetition rate of ~ 80 fs and 1–8 MHz, respectively. Intensities were monitored at 1.85 eV and detected using an avalanche photodiode detector (ID-100-MMF50-ULN, Becker & Hickl) with 40 ps timing resolution and a sensitivity range of 300–900 nm. To keep the condition of weak optical excitation during TRPL measurement, the density of photons per pulse was

maintained as 10^9 photons \cdot cm^{-2} \cdot pulse $^{-1}$, which corresponds to an excess carrier density, Δn of $\approx 10^{13}$ cm^{-3} .

A three-electrode standard setup was used for PEC measurements. Electrolyte consists of 0.4 mol l^{-1} K_2HPO_4 , 0.4 mol l^{-1} KH_2PO_4 , and 0.4 mol l^{-1} K_2SO_4 with pH = 6.84. A Pt wire and Ag/AgCl were used as the counter and reference electrodes, respectively. A high-brightness 500 W xenon lamp (XEF-501S) was used for illuminating the FTO side in the J - V measurements. The J - V curves were scanned from -0.2 to 0.8 V (versus Ag/AgCl) using a potentiostat (Hokuto Denko HSV-110).

3. Results and discussion

3.1. XPS analysis

Figure 2(a) shows the XPS spectra of the undoped and sulfur-doped BiVO_4 thin films. The atomic ratios of Bi, V, O, and S, calculated from the peak area of the high-resolution XPS spectra, suggest that the sulfur content in the films varied from 8 at% to 11 at%. Accordingly, we defined the sample names as S_8 - BiVO_4 , S_{10} - BiVO_4 and S_{11} - BiVO_4 corresponding to sulfur incorporation of ~ 8 at%, ~ 10 at%, and ~ 11 at%, respectively. S2s peaks of S_8 - BiVO_4 and S_{10} - BiVO_4 films with a binding energy of ~ 232.5 eV [Fig. 2(b)] can be assigned to S^{2-} species in BiVO_4 .^{20,23–25} The S2s peak of the S_{11} - BiVO_4 sample in the higher binding energy region (~ 236 eV) compared to the peak lower binding energy position (~ 233.2 eV) may be assigned as S_8 ²⁶ or sulphate (SO_4) and sulfide (S^{2-}).^{27–29} respectively. The peak shift in the S_{11} - BiVO_4 sample, at ~ 233.2 eV, can be estimated by the changes in the band gap by doping sulfur into BiVO_4 . Figure 2(c) shows $\text{Bi}4f_{7/2}$ and $\text{Bi}4f_{5/2}$ symmetric peaks at 158.9 and 164.2 eV, respectively, which are the characteristic peaks for Bi^{3+} .^{30,31} The small positive shift in the $\text{Bi}4f$ peaks by sulfur doping in BiVO_4 may be originated from the decrease in the electron cloud density around Bi.³² A similar trend was observed for the V2p peak. The decrease in the $\text{Bi}4f$ peaks due to sulfur doping in BiVO_4 suggests that S^{3p} introduces defects in the VB of BiVO_4 .

The XPS spectra corresponding to the $\text{V}2p_{3/2}$ and O1s binding energies are shown in Fig. 2(d). $\text{V}2p_{3/2}$ at 516.7 eV is assigned to surface V^{5+} species³⁰ and is ascribed to the oxide form of V in BiVO_4 .³³ O1s spectra of all samples were obtained with two different subpeaks of O^{2-} : oxygen lattice (O_{lat}) at 529.7 eV and a peak at 532.1 eV assigned to the oxygen vacancy.³⁴ The O1s peak shifted to higher binding

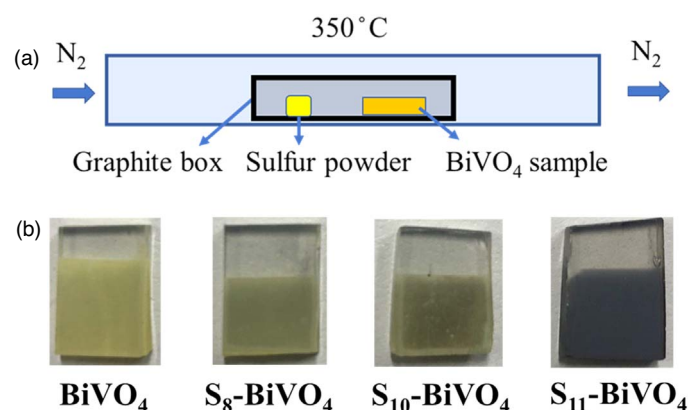


Fig. 1. Schematic of sulfurization process (a), undoped and sulfur-doped BiVO_4 samples with various doping concentrations through sulfurization (b).

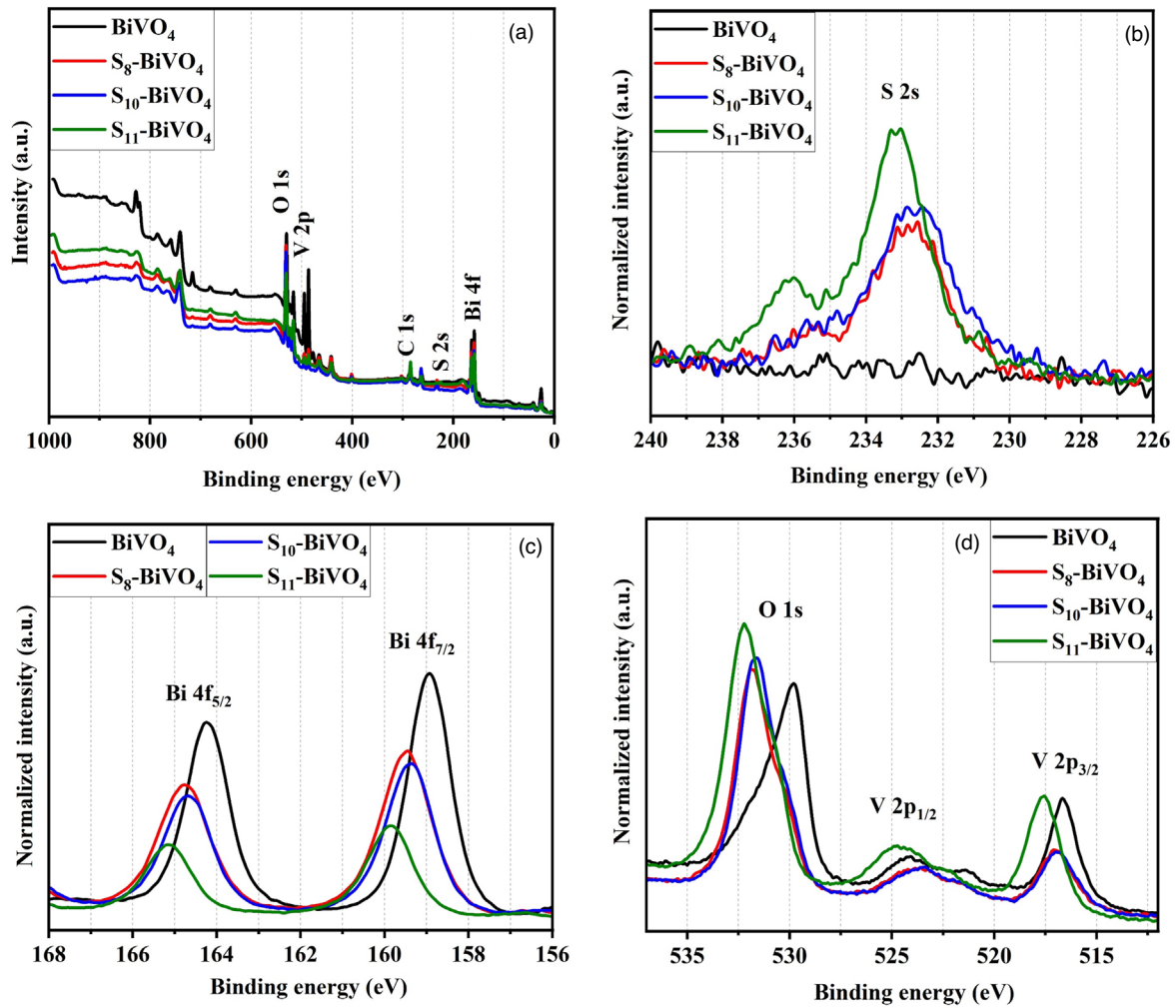


Fig. 2. XPS spectra (a), high-resolution XPS spectra of S2s (b), Bi4f (c), V2p, and O1s (d) of BiVO₄ and sulfur-doped BiVO₄ thin films.

energy (532.1 eV) by sulfur doping in BiVO₄, possibly due to its high electron-attracting effect.³⁴⁾ The presence of more oxygen vacancies in the crystal structure may be the cause of the SO₄⁻ formation.³⁵⁾ Oxygen vacancies can reduce electron-hole recombination by the electron capturing center to enhance the transfer of trapped electrons.³⁶⁾ High electron density can be created in the VB due to oxygen defects; this might be advantageous for enhancing the PEC performance of BiVO₄ thin films by increasing the probability of absorbed electron's transfer from the VB to the conduction band.

3.2. Structural analysis

XRD patterns of sulfur-doped BiVO₄ thin films on the FTO substrates are shown in Fig. 3(a). In general, all the samples showed similar crystal structures, which can be indexed to monoclinic BiVO₄ (JCPDS card no. 14-0688). However, the S₁₁-BiVO₄ film showed a mixed impurity phase of Bi₂S₃ (JCPDS card no. 170320) and monoclinic BiVO₄. Figure 3(b) shows magnified and normalized XRD peaks of (121) and (004) planes at approximately 29.06° and 30.72°, respectively, for BiVO₄ and sulfur-doped BiVO₄ thin films. XRD measurements did not detect any shift in the peaks of the S₈-BiVO₄ sample comparable to the peaks in those of undoped BiVO₄. However, the S₁₀-BiVO₄ sample shows a shift in the (121) peak, which is the dominant plane in the monoclinic BiVO₄ structure. A slight shift in the XRD peak due to sulfur doping into BiVO₄ toward a lower

diffraction angle suggests the presence of S²⁻ ions in BiVO₄. According to Bragg's law, the diffraction peak shift to a lower angle can be attributed to the higher ionic radius (0.184 nm) of sulfur than that of oxygen (0.140 nm). Thus, the substitution of oxygen with sulfur increases the lattice parameter.²³⁾ The Scherrer equation [Eq. (1)] was used to calculate the crystallite size from the (121) peak.

$$D = \frac{K\lambda}{\beta \cos \theta} \tag{1}$$

where $K = 0.89$, λ is the X-ray wavelength (0.1541 nm), β is the FWHM, and θ is half of the diffraction angle. The crystallite sizes of BiVO₄, S₈-BiVO₄, and S₁₀-BiVO₄ were 47.10, 43.73, and 34.01 nm, respectively. Sulfur doping led to a decrease in the crystallite size of BiVO₄; similar results have been reported in other studies.²³⁾ The significant decrease in peak intensity and peak shift of the (121) index in the S₁₁-BiVO₄ sample suggest that a high sulfur dopant concentration might distort the crystal structure of BiVO₄, as highlighted by the XPS results. Considering the XPS S2s peak and XRD pattern of the S₁₁-BiVO₄ sample, sulfur doping into BiVO₄ has a limitation: high doping of sulfur results in distortion in the lattice of BiVO₄.

To distinguish the structural form in bulk (from XRD results) and on the surface of undoped and sulfur-doped BiVO₄ thin films, the Raman spectra of the samples were

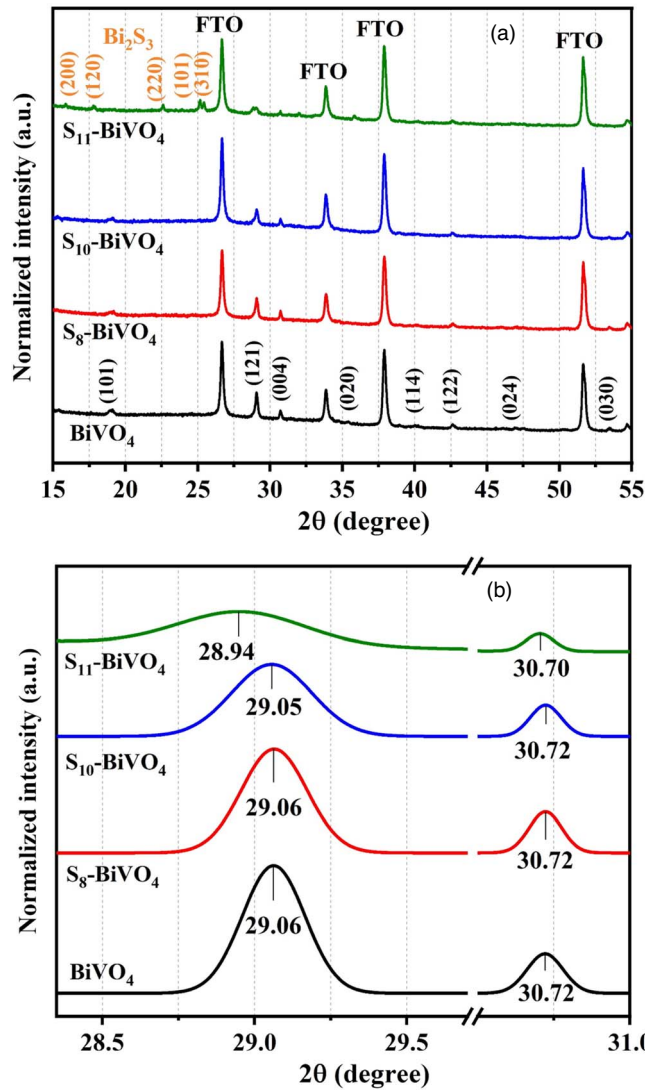


Fig. 3. XRD patterns of BiVO₄ and sulfur-doped BiVO₄ thin films on the FTO substrate. (a) Wide-angle XRD pattern and (b) detailed range of XRD patterns for peaks corresponding to (121) and (004) planes at approximately 29.06° and 30.72°, respectively.

analyzed. As shown in Fig. 4(a), the recorded Raman spectra of all samples exhibit characteristic peaks of monoclinic BiVO₄, consisting of a stretching vibration (ν_s) at 827 cm⁻¹ and an asymmetric vibration mode (ν_{as}) at 706 cm⁻¹ corresponding to V–O bonds. The highest sulfur-doped film (S₁₁-BiVO₄) had very low Raman signals, originating from the V–O vibration in BiVO₄. This is assumed to be the decreasing quantity of V–O bonds of the BiVO₄ owing to the formation of a secondary phase in the film (XRD of S₁₁-BiVO₄). Peak shifts are observed at lower wavenumbers in sulfur-doped BiVO₄ films at ~825 cm⁻¹ compared to those in pure BiVO₄ at 827 cm⁻¹ [Fig. 4(b)]. Raman peak shift can be created by S doping into metal oxides due to formation defects states and changing oxygen vacancies.³⁷⁾ Shift in the stretching vibration ν_s (V–O) in BiVO₄ thin films by sulfur doping suggests that S²⁻ is partially substituted in O²⁻ sites.

3.3. Optical characterization

The optical bandgaps of BiVO₄ and sulfur-doped BiVO₄ thin films were obtained using transmittance and reflectance spectra.

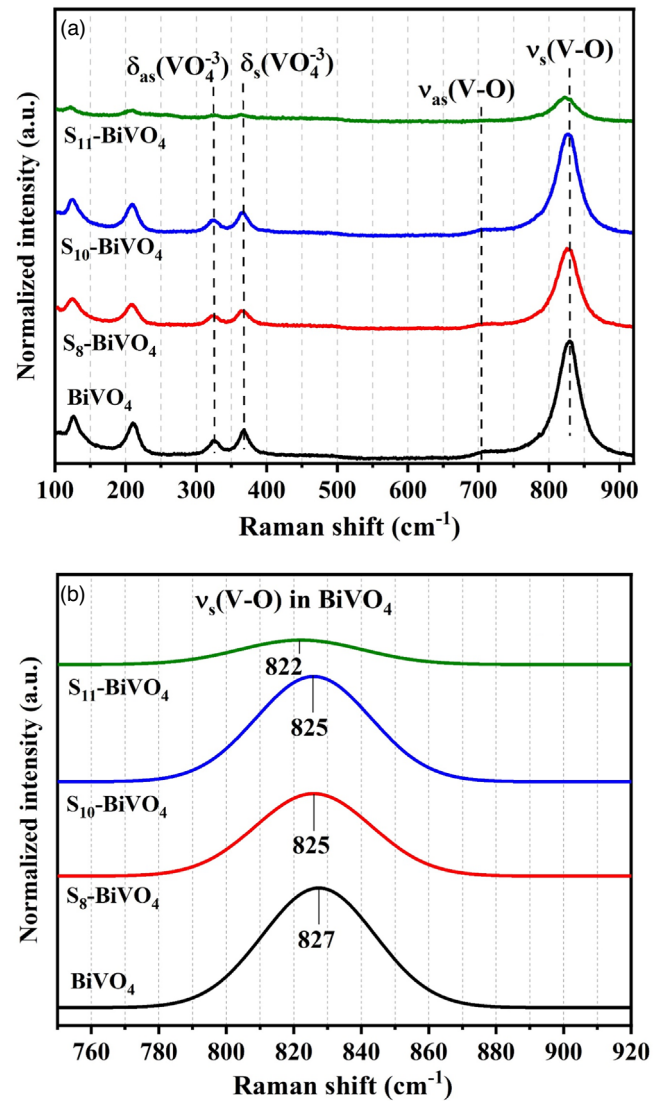


Fig. 4. Raman spectra of BiVO₄ and sulfur-doped BiVO₄ thin films (a). Normalized stretching vibration ν_s (V–O) (b).

The optical absorption coefficient, α was calculated by:

$$\alpha = \frac{1}{d} \ln \left(\frac{1 - R^2}{T} \right) \quad (2)$$

where d is the thickness of the thin film, T and R are the transmittance and reflectance, respectively. The optical bandgap of the thin films was estimated using the Tauc plot, based on Eq. (3), which is given by

$$(\alpha h\nu)^n = A \cdot (h\nu - E_g) \quad (3)$$

where $h\nu$ is the photon energy, E_g is the transition energy, and A is the proportionality constant. n equals $\frac{1}{2}$ because BiVO₄ is an indirect bandgap semiconductor.³⁸⁾ Further, $(\alpha h\nu)^{1/2}$ versus $h\nu$ allows the determination of the optical bandgap energy of the samples. Figure 5 shows that the optical bandgap of BiVO₄ is ~2.48 eV, where sulfur-doped BiVO₄ thin films show a narrower bandgap than BiVO₄. The absorption of the pure BiVO₄ sample begins at ~2.3 eV. However, sulfur-doped thin films exhibit light absorption below ~1.6 eV. As mentioned in the introduction, S3p states mixed with O2s states introduce oxygen defects in the VB,

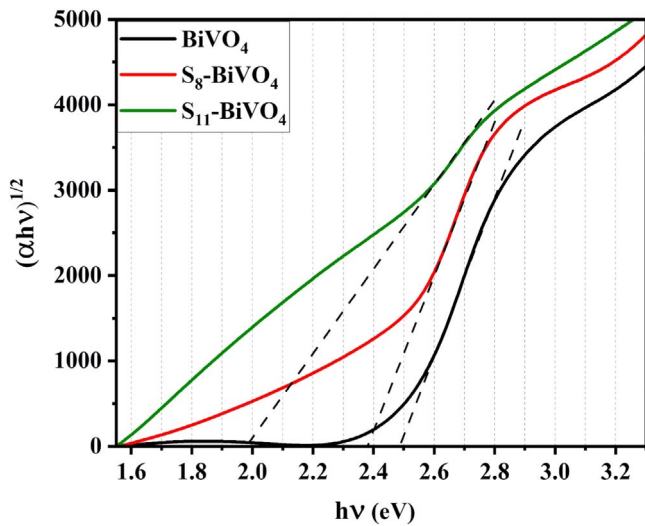


Fig. 5. Tauc plots for BiVO₄ and sulfur-doped BiVO₄ thin films, along with linear fits of the absorption edges.

shifting the electron density states upward, thereby causing absorption with low-energy photons.

3.4. PEC characterization

PEC measurements were conducted using a three-electrode setup. The Xe lamp was set to approximately 1 sunlight irradiation as a source of back-side illumination of the samples. The potentials were converted to the reversible hydrogen electrode scale using the Nernst equation:

$$E_{RHE} = E_{Ag/AgCl} + 0.197 + 0.059 \cdot \text{pH} \quad (4)$$

Figure 6(a) illustrates the photocurrent density of the BiVO₄ and sulfur-doped BiVO₄ thin films. The S₈-BiVO₄ sample showed the highest PEC performance, where the S₁₀-BiVO₄ photocurrent density was higher than that of pure BiVO₄. It can be considered that the formation of the oxygen vacancy, by sulfur doping in BiVO₄, may play an important role in the charge transfer procedure. Since no XRD peak of the impurity phase in S₈-BiVO₄ and S₁₀-BiVO₄ films, the partial existence of SO₄ on the surface may not affect the PEC properties of BiVO₄. The highly sulfur-doped S₁₁-BiVO₄ exhibited the lowest charge separation among all the samples. It is supposed that structural change of BiVO₄ results in PEC performance deterioration.

To understand the mechanism for improved photocurrent in sulfur-doped samples, we measured steady-state PL of undoped BiVO₄ and sulfur-doped BiVO₄ with two different laser sources (wavelength of 400 nm and 532 nm, which correspond to the energy of ~3.1 eV and ~2.33 eV, respectively). A PL peak around 1.85 eV has been found in both undoped and sulfur-doped samples, measured with both wavelengths [Supplementary Information (SI) Fig. S1.].

Previously, our group studied temperature and excitation power dependent on ~1.85 eV PL peaks in BiVO₄ samples.³⁹ The origin of the 1.85 eV peak has been assigned as donor-acceptor pair recombination from shallow acceptors (35 eV and 115 eV above valance band) and deep donors (575 eV and 655 eV below conduction band). Thus, photocarrier recombination was assumed to occur through multiphonon nonradiative recombination, via deep traps. Details of the PL results have been discussed in SI. In this study, later, to measure the effective lifetime of minority carriers in BiVO₄, we measured

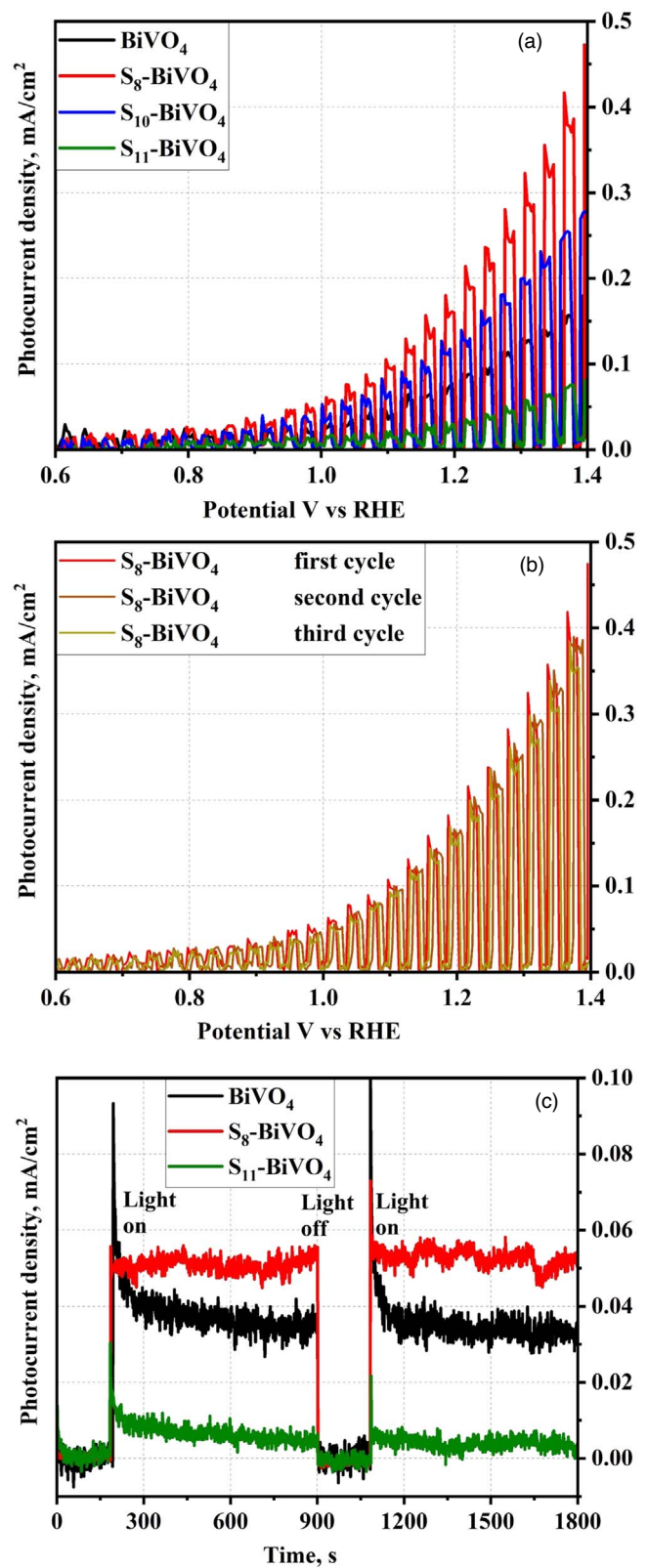


Fig. 6. LSV scan photocurrent of BiVO₄ and sulfur-doped BiVO₄ films on FTO glass substrates (a), three-cycle LSV scan of S₈-BiVO₄ sample with the 15 min gap (b), test photocurrent stability of BiVO₄ and sulfur-doped BiVO₄ films in 1.0 V_{RHE}.

TRPL by monitoring the luminescence decay at 1.85 eV as a function of time (SI, Fig. S3.). For TRPL measurement, we have considered undoped BiVO₄ and sulfur-doped samples (S₈-BiVO₄). Observed minority-carrier lifetime has similarly been found, $\tau \approx 9$ ns for both pure and sulfur-doped BiVO₄

which is assumed as a nonradiative recombination lifetime due to the Shockley–Read–Hall (SRH) recombination. However, an almost equal lifetime of sulfur-doped BiVO_4 with pure one, suggests no changes with recombination constant and equilibrium concentrations of holes.

Thus, although further investigation is necessary with variable-wavelength experiments, such as incident photon-to-current efficiency, from the above discussion, it can be roughly assumed that the improved PEC performance of the sulfur-doped samples ($\text{S}_8\text{-BiVO}_4$) may be resulted from the absorption of longer-wavelength light due to the decrease in bandgap energy, rather than changes in film quality, that contributes to the increase in photocurrent.

Three-cycle linear sweep voltammogram (LSV) scans of the $\text{S}_8\text{-BiVO}_4$ sample with a gap of 15 min were performed to check the stability of the thin film for photocatalytic activity [Fig. 6(b)]. The $\text{S}_8\text{-BiVO}_4$ sample almost did not change its photocurrent stability after 30 min under light illumination. A test of photocurrent stability has been provided and compared for pure and sulfur-doped BiVO_4 samples in 1.0 V_{RHE} [Fig. 6(c)]. BiVO_4 and $\text{S}_8\text{-BiVO}_4$ samples illustrated almost stable photocurrent. $\text{S}_{11}\text{-BiVO}_4$ samples have a miniature photocurrent, and it has been decreased by 30 min illumination. Figure 7 shows XPS and XRD comparable data before and after the PEC measurement of the $\text{S}_8\text{-BiVO}_4$ sample. XPS wide scan spectrum illustrated the S2s peak slightly decreased post-PEC [Fig. 7(a)] and note that high-resolution XPS did not detect S2s, probably, because of weak signal from the S2s state. Post-PEC XRD of the $\text{S}_8\text{-BiVO}_4$ sample is shown in Fig. 7(b). Extra peaks have been obtained after PEC (mentioned as *), which is not related to monoclinic BiVO_4 . Those peaks are not assigned as XRD peaks of Bi and/or V contain crystal phase. However, the impact of electrolyte on the thin film can be the reason for the occurrence of unknown peaks after the PEC test.^{40,41} Both differences of pre and post-PEC of $\text{S}_8\text{-BiVO}_4$ sample in XPS spectra and XRD data, speculated by interface interaction between the sample and electrolyte. PEC measurements confirmed that sulfur doping increased the photocurrent of the BiVO_4 thin films. A large amount of doping can lead to structural changes in the film and decrease PEC performance. Accurate control of sulfur doping is required to optimize the doping concentration of sulfur into the BiVO_4 structure to achieve the best PEC performance.

4. Conclusions

BiVO_4 thin films were deposited from a single target using RF sputtering. Various concentrations of sulfur were doped into the BiVO_4 structure by the post-deposition sulfurization method. XPS analysis confirmed the incorporation of sulfur in the host BiVO_4 crystal, mainly through the successful substitution of O^{2-} with S^{2-} . Structural analysis performed by XRD also confirmed the incorporation of sulfur into BiVO_4 , which manifested as a shift in the dominant (121) peak, mainly due to the difference in the ionic radius of substituting sulfur compared to oxygen. Sulfur doping with $\sim 8\%$ in BiVO_4 film showed the best PEC performance with stable photocurrent, which can be concluded as accurate control of a small amount of sulfur doping that can be effective for BiVO_4 photoanode. The obtained results show that a large amount of sulfur incorporation distorts the BiVO_4 local structure in addition to the generation of impurity

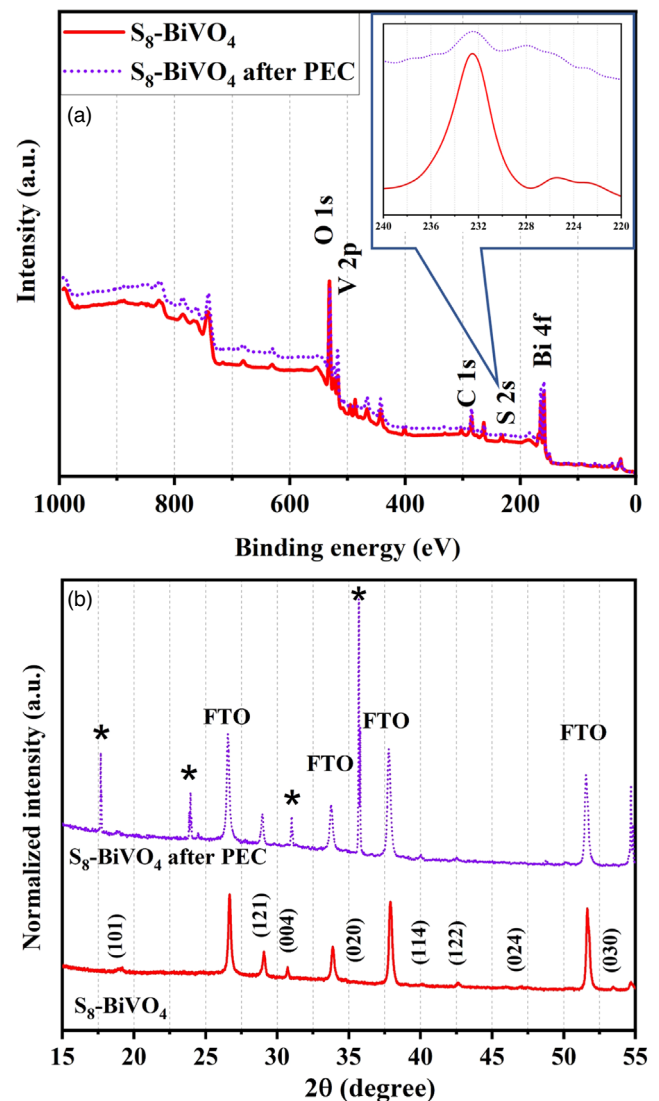


Fig. 7. Comparison of XPS (a) and XRD (b) data of the $\text{S}_8\text{-BiVO}_4$ pre (red line) and post-PEC measurement (purple, dots).

phases, as confirmed by XRD and Raman spectroscopy. Consequently, a decrease is observed in the photocatalytic activity of the highly sulfur-doped samples. Further, optimization of sulfur doping at a lower concentration might be required to further improve PEC performance.

Acknowledgments

This work was supported by Grants-in-Aid for Scientific Research (KAKENHI) of the Japan Society for the Promotion of Science (JSPS, Awards No. 19H02656, 19H02822, and 20H05120).

ORCID iDs

Shukur Gofurov <https://orcid.org/0000-0002-5456-8182>

Muhammad M. Islam <https://orcid.org/0000-0002-9448-731X>

Takeaki Sakurai <https://orcid.org/0000-0001-5730-1937>

1) A. Fujishima and K. Honda, *Nature* **238**, 37 (1972).

2) R. Asahi, T. Morikawa, T. Ohwaki, K. Aoki, and Y. Taga, *Science* **293**, 269 (2001).

- 3) M. Sarnowska, K. Bienkowski, P. J. Barczuk, R. Solarzka, and J. Augustynski, *Adv. Energy Mater.* **6**, 1600526 (2016).
- 4) H. S. Han, S. Shin, D. H. Kim, I. J. Park, J. S. Kim, P.-S. Huang, J.-K. Lee, I. S. Cho, and X. Zheng, *Energy Environ. Sci.* **11**, 1299 (2018).
- 5) J. H. Kim, J.-W. Jang, Y. H. Jo, F. F. Abdi, Y. H. Lee, R. van de Krol, and J. S. Lee, *Nat. Commun.* **7**, 13380 (2016).
- 6) J. H. Kim and J. S. Lee, *Adv. Mater.* **31**, 1806938 (2019).
- 7) A. J. E. Rettie, H. C. Lee, L. G. Marshall, J.-F. Lin, C. Capan, J. Lindemuth, J. S. McCloy, J. Zhou, A. J. Bard, and C. Buddie Mullins, *J. Am. Chem. Soc.* **135**, 11389 (2013).
- 8) Y. Hermans, A. Klein, K. Ellmer, R. Krol, T. Toupance, and W. Jagermann, *J. Phys. Chem. C* **122**, 20861 (2018).
- 9) M. Shang, W. Wang, J. Ren, S. Sun, and L. Zhang, *CrystEngComm* **12**, 1754 (2010).
- 10) L. Hou, L. Yang, J. Li, J. Tan, and C. Yuan, *J. Anal. Methods Chem.* **2012**, 345247 (2012).
- 11) D. K. Lee, D. Lee, M. A. Lumley, and K.-S. Choi, *Chem. Soc. Rev.* **48**, 2126 (2019).
- 12) A. Kudo, K. Ueda, H. Kato, and I. Mikami, *Catal. Lett.* **53**, 229 (1998).
- 13) S. Tokunaga, H. Kato, and A. Kudo, *Chem. Mater.* **13**, 4624 (2001).
- 14) K. E. Kweon and G. S. Hwang, *Phys. Rev. B: Condens. Matter Mater. Phys.* **86**, 165209 (2012).
- 15) Y. Pihosh et al., *Sci. Rep.* **5**, 11141 (2015).
- 16) T. W. Kim, Y. Ping, G. A. Galli, and K.-S. Choi, *Nat. Commun.* **6**, 8769 (2015).
- 17) A. Iwase, S. Nozawa, S. Adachi, and A. Kudo, *J. Photochem. Photobiol. A* **353**, 284 (2018).
- 18) B. Pattengale, J. Ludwig, and J. Huang, *J. Phys. Chem. C* **120**, 1421 (2016).
- 19) Z. Pan, J. A. Röhr, Z. Ye, Z. S. Fishman, Q. Zhu, X. Shen, and S. Hu, *Sustain. Energy Fuels* **3**, 850 (2019).
- 20) M. Lamers et al., *Chem. Mater.* **30**, 8630 (2018).
- 21) S. Gahlawat, P. Schnell, R. Irani, I. Y. Ahmet, L. Choubrac, S. Fiechter, P. P. Ingole, and F. F. Abdi., *Sol. RRL* **6**, 2200129 (2022).
- 22) Y. R. Luo, *Comprehensive Handbook of Chemical Bond Energies* (CRC Press, Boca Raton, FL, 2007) Vol. 55.
- 23) M. Guo, Y. Wang, Q. He, W. Wang, W. Wang, Z. Fu, and H. Wang, *RSC Adv.* **5**, 58633 (2015).
- 24) Z. Zhao, H. Dai, J. Deng, Y. Liu, and C. Tong, *Chin. J. Catal.* **34**, 1617 (2013).
- 25) V. H. Nguyen, Q. T. P. Bui, D.-V. N. Vo, K. T. Lim, L. G. Bach, S. T. Do, T. V. Nguyen, V.-D. Doan, T.-D. Nguyen, and T. D. Nguyen, *Materials* **12**, 2681 (2019).
- 26) H.-P. Jiao, X. Yu, Z.-Q. Liu, P.-Y. Kuang, and Y.-M. Zhang, *RSC Adv.* **5**, 16239 (2015).
- 27) M. Miodynska, A. Mikolajczyk, B. Bajorowicz, J. Zwara, T. Klimczuk, W. Lisowski, G. Trykowski, H. P. Pinto, and A. Zaleska-Medynska, *Appl. Catal. B* **272**, 118962 (2020).
- 28) A. Naumkin, A. Kraut-Vass, S. Gaarenstroom, and C. Powell, (2012).
- 29) Y. Wang, Y. Wang, Y. Meng, H. Ding, Y. Shan, X. Zhao, and X. Tang, *J. Phys. Chem. C* **112**, 6620 (2008).
- 30) H. Jiang, H. Dai, X. Meng, K. Ji, L. Zhang, and J. Deng, *Appl. Catal. B* **105**, 326 (2011).
- 31) M. Wang, C. Niu, J. Liu, Q. Wang, C. Yang, and H. Zheng, *J. Alloys Compd.* **648**, 1109 (2015).
- 32) L. G. Devi and R. Kavitha, *Mater. Chem. Phys.* **143**, 1300 (2014).
- 33) A. Zhang and J. Zhang, *J. Alloys Compd.* **491**, 631 (2010).
- 34) A. B. Abdeta, Q. Wu, D.-H. Kuo, P. Li, H. Zhang, T. Huang, J. Zhang, J. Lin, and X. Chen, *J. Catal.* **413**, 1056 (2022).
- 35) B. J. Lindberg, K. Hamrin, G. Johansson, U. Gelius, A. Fahlman, C. Nordling, and K. Siegbahn, *Phys. Scr.* **1**, 286 (1970).
- 36) S. Jin, X. Ma, J. Pan, C. Zhu, S. E. Saji, J. Hu, X. Xu, L. Sun, and Z. Yin, *Appl. Catal. B: Environ.* **281**, 119477 (2021).
- 37) H. Rasoulnezhad, G. Hosseinzadeh, and J. Yekrang, *J. Nanostruct.* **8**, 251 (2018).
- 38) J. K. Cooper, S. Gul, F. M. Toma, L. Chen, Y.-S. Liu, J. Guo, J. W. Ager, J. Yano, and I. D. Sharp, *J. Phys. Chem. C* **119**, 2969 (2015).
- 39) I. Abdellaoui et al., *J. Phys. Chem. C* **124**, 3962 (2020).
- 40) M. Shaban, A. Almohammed, R. Saad, and A. M. El Sayed, *Nanomaterials* **12**, 453 (2022).
- 41) M. T. Galante et al., *ACS Appl. Mater. Interfaces* **13**, 32865 (2021).